SANDIA REPORT
SAND2014-3539
Unlimited Release
Printed April 2014

Defect Localization, Characterization and Reliability Assessment in Emerging Photovoltaic Devices

Benjamin B. Yang, Jose Luis Cruz-Campa, Gaddi S. Haase, Paiboon Tangyunyong, Edward J. Cole, Jr., Murat Okandan, Gregory N. Nielson

Prepared by
Sandia National Laboratories
Albuquerque, New Mexico 87185 and Livermore, California 94550

Sandia National Laboratories is a multi-program laboratory managed and operated by Sandia Corporation, a wholly owned subsidiary of Lockheed Martin Corporation, for the U.S. Department of Energy's National Nuclear Security Administration under contract DE-AC04-94AL85000.

Sandia National Laboratories

Issued by Sandia National Laboratories, operated for the United States Department of Energy by Sandia Corporation.

Printed in the United States of America. This report has been reproduced directly from the best available copy.

Available to DOE and DOE contractors from
U.S. Department of Energy
Office of Scientific and Technical Information
P.O. Box 62
Oak Ridge, TN 37831

Telephone: (865) 576-8401
Facsimile: (865) 576-5728
E-Mail: reports@adonis.osti.gov
Online ordering: http://www.osti.gov/bridge

Available to the public from
U.S. Department of Commerce
National Technical Information Service
5285 Port Royal Rd.
Springfield, VA 22161

Telephone: (800) 553-6847
Facsimile: (703) 605-6900
E-Mail: orders@ntis.fedworld.gov
Online order: http://www.ntis.gov/help/ordermethods.asp?loc=7-4-0#online

SAND2014-3539
Unlimited Release
Printed April 2014

Defect Localization, Characterization and Reliability Assessment in Emerging Photovoltaic Devices

Benjamin B. Yang[1], Jose Luis Cruz-Campa[2], Gaddi S. Haase[1], Paiboon Tangyunyong[1],
Edward I. Cole, Jr.[3], Murat Okandan[2], Gregory N. Nielson[2]
[1]Validation and Failure Analysis Department
[2]MEMS Technologies Department
[3]Science and Technology Division
Sandia National Laboratories
P.O. Box 5800, MS 1081
Albuquerque, New Mexico 87185-1081

Abstract

Microsystems-enabled photovoltaics (MEPV) can potentially meet increasing demands for light-weight, portable, photovoltaic solutions with high power density and efficiency. The study in this report examines failure analysis techniques to perform defect localization and evaluate MEPV modules. CMOS failure analysis techniques, including electroluminescence, light-induced voltage alteration, thermally-induced voltage alteration, optical beam induced current, and Seabeck effect imaging were successfully adapted to characterize MEPV modules. The relative advantages of each approach are reported. In addition, the effects of exposure to reverse bias and light stress are explored. MEPV was found to have good resistance to both kinds of stressors. The results form a basis for further development of failure analysis techniques for MEPVs of different materials systems or multi-junction MEPVs. The incorporation of additional stress factors could be used to develop a reliability model to generate lifetime predictions for MEPVs as well as uncover opportunities for future design improvements.

ACKNOWLEDGMENTS

The principal investigator of this project would like to thank the various individuals that helped make this project and its outcomes possible. Jose Luis Cruz-Campa, Greg Nielson, and Murat Okandan have been instrumental to the development of the project's proposal and their advice, expertise, and samples contributed to the heart of the study. Gaddi S. Haase, Paiboon Tangyunyong, Edward J. Cole Jr., and Mary Miller provided precious time and crucial failure analysis and reliability knowledge.

A heartfelt thanks also goes out to the various managers that championed the project and brought it into fruition. David Stein, Fred Sexton, and Guillermo Loubriel provided continuous support, enthusiasm, and encouragement throughout the shuffling of direct management positions that occurred during the proposal process. The efforts of Gilbert Herrera and Wahid Hermina to make this project a reality are also greatly appreciated.

CONTENTS

FIGURES

TABLES

NOMENCLATURE

A	amperes (unit)
AC	alternating current
CAD	computer aided design
CCD	charge-coupled device
cm	centimeter (10^{-2} meters) (unit)
CMOS	complementary metal-oxide semiconductor
DC	direct current
EL	electroluminescence
FIB	focused ion beam
IBC	interdigitated back contact
IV	current (I) - voltage (V)
LDRD	Laboratory-Directed Research and Development
LEM	light emission microscopye
LID	light-induced degradation
LIVA	light-induced voltage alteration
MEPV	microsystems-enabled photovoltaics
μA	microamperes (10^{-6} amperes) (unit)
μm	microns / micrometers (10^{-6} meters) (unit)
mm	millimeter (10^{-3} meters) (unit)
nm	nanometer (10^{-9} meters) (unit)
OBIC	optical beam induced current
PV	photovoltaics
SEI	Seabeck effect imaging
SEM	scanning electron microscopy
TIVA	thermally-induced voltage alteration
V	volts (unit)

1. INTRODUCTION

Photovoltaic (PV) technologies are rapidly becoming an increasingly important source of renewable power source for a broad range of applications. In particular, PV power sources are a potential solution to meet demand for remote, portable power. These applications value low weight, flexible substrate capability, and good efficiency.

Microsystems-enabled photovoltaics (MEPV) are a promising approach that could satisfy the previous requirements for remote, portable power. MEPV utilizes microfabrication techniques to fabricate small PV cells that are less than 1 millimeter (mm) in diameter and approximately 20 micrometers (μm) in thickness. This and similar microsystems-based approaches create several scaling advantages that lead to high power density by weight, the ability to package onto flexible substrates, improved carrier collection efficiency [1]–[3].

Rapid maturation of MEPV benefits from the development of failure analysis techniques and reliability studies, executed in conjunction with investments in device design and fabrication. The microfabricated origins of MEPV results in feature sizes that are smaller than dimensions found in traditional PV. These length scales are familiar territory for traditional microelectronics failure analysis tools. The electrical behavior of MEPV, however, differs from conventional complementary metal-oxide semiconductor (CMOS) devices found in microelectronics. As such, adjustments are necessary when translating these tools to applications in MEPV.

This SAND report describes the primary findings throughout an effort to adapt CMOS failure analysis tools to evaluate MEPV cells. In addition, this document also discusses studies on the effects of reverse bias stress and light induced stress on the electrical characteristics of MEPV. These two sources of stress are gaining increased attention in the PV community. Reverse bias stress is commonly experienced by PV modules that experience partial shading. Light-induced degradation (LID) is a phenomenon that has been observed in single-crystalline, boron-doped, Czochralski-grown silicon that lowers efficiency of PV cells after prolonged exposure to light.

The study finds CMOS failure analysis techniques to be well-suited for MEPV defect localization after some minor adjustments described in this report. Further examination also found MEPV to be resilient to reverse bias stress and the effects of LID. The results of this report form the basis for further development of failure analysis tools targeted towards multi-junction MEPVs and detailed quantification of these devices to a broader range of stressors. While these findings are specific to MEPV devices, the failure analysis techniques described are applicable to any researcher using novel techniques to scale down PV device dimensions.

1.1. MEPV Overview

This study focuses on silicon MEPV, which are fabricated on 6-inch, 20-30 Ω-cm, p-type, (100)-oriented, silicon-on-insulator wafers with a 20 μm device layer and a 1 μm buried oxide layer. The devices have an interdigitated back contact (IBC) metal layer underneath, which are connected to silicon regions that are doped p-type or n-type, depending on the contact in question [4].

Figure 1 is a computer aided design (CAD) drawing that shows the layout of the IBC and the implantation regions in an MEPV. The light-green geometry outlines the shape of the IBC, which is split into two halves. The left half is connected to circular regions that are implanted to be n-type with phosphorous. The right half is connected to similar areas that are implanted to be p-type with boron. The connections between the IBC and the implantation regions are made through 3-μm-diameter contacts shown as black dots in the figure.

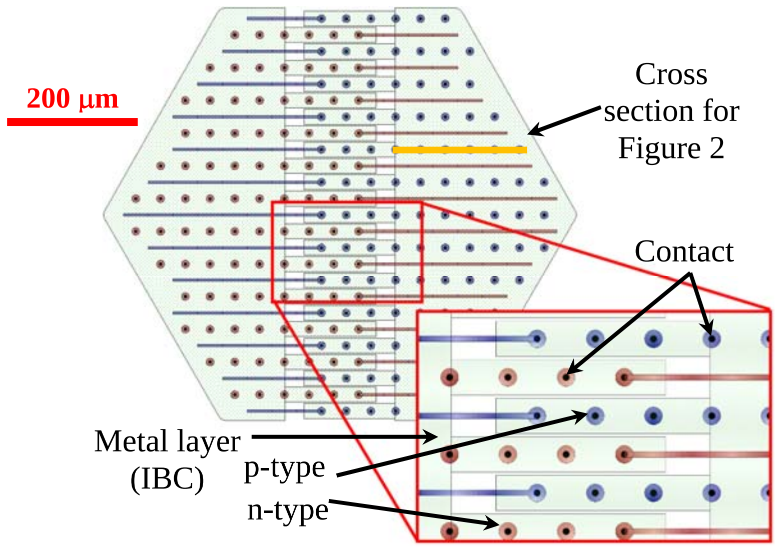

Figure 1: A computer aided design (CAD) drawing that illustrates the doping profile and interdigitated back contact (IBC) metal layer. The areas doped p-type are represented in blue and the areas doped n-type are represented in brown. The black dots, visible in the magnified view, represent the contacts that connect the p-type and n-type areas to their respective electrode in the IBC layer.

Figure 2 depicts a cross section along the p-type region of the MEPV as indicated by the orange line in Figure 1. The figure is not drawn to scale for illustration purposes and serves as an appropriate visual aid to describe the MEPV fabrication process. The MEPV initially has an orientation that is upside-down to that of Figure 2 while on the original silicon-on-insulator handling wafer. Boron and phosphorous are first implanted in accordance to the CAD layout in Figure 1. A nitride layer is then deposited and etched to form the contacts that will connect the silicon with the IBC. Next, the IBC is deposited along with a final nitride layer. The nitride is etched and four copper pillars (also shown in Figure 3) are electroplated onto the IBC that later form the connection between the IBC and final substrate. Once these fabrication steps are complete, the MEPV cell is released from its handling wafer, flipped over, and deposited in the final silicon-side-up, metal-side-down configuration shown in Figure 2.

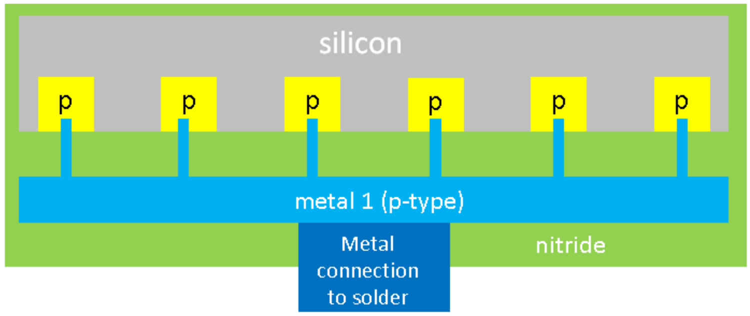

Figure 2: Cross section sketch of the p-type portion of the MEPV cell in its final configuration with the silicon-side-up and metal-side-down. The p-type implant islands are visible, as well as the contacts that connect these regions to the metal layer underneath. Silicon nitride separates the metal layer from the silicon and also serves as additional protection. The cells are interconnected on the final substrate through electroplated copper attached with solder.

Figure 3 shows a bright field image of an MEPV cell in the metal-side-up, silicon-side-down orientation prior to release from its handle wafer. The two halves of the IBC are shown as well as the four electroplated metal connections that are soldered onto the final substrate. Also visible as small black dots are the etch release holes that were not shown in previous figures. The etch release holes facilitate the wet etch release step that removes most of the physical connections between the MEPV and the handling wafer.

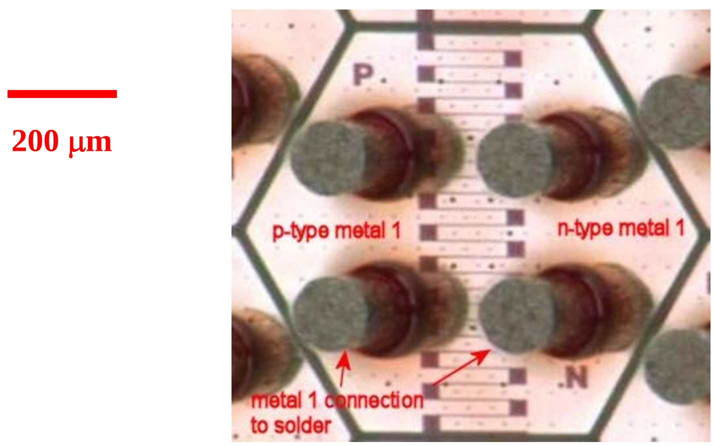

Figure 3: Backside (metal-side-up, silicon-side-down) bright field image of an MEPV cell. The metal IBC layer, which constitutes a majority of the visible surface in the figure, is split into two interdigitated halves. The left half, labeled with the letter "P," is connected to p-doped islands in the silicon. The right half, labeled with the letter "N," is connected to the n-doped islands in the silicon. The silicon is visible beneath the metal layer between the interdigitated fingers. The four pillars shown provide electrical connection to the substrate through a solder connection in a subsequent packaging step. Also visible are etch-release holes that assist with the separation of the MEPV cell from the substrate wafer.

Sample photographs of MEPVs that were packaged on both rigid (left) and flexible (right) substrates are shown in Figure 4. The cells are connected in parallel along the longer, horizontal, dimension and each row is then connected in series. The interconnection between the cells is made on the packaging substrate, which allows mass production of identical MEPV cells that can then be placed on different application-specific substrates that result in the appropriate output voltage and current. The right-side image of Figure 4 also demonstrates the ability to apply MEPV on flexible substrates, with a demonstrated bending radius of approximately 1 mm. At this bending radius, the cells are unaffected by the substrate curvature and are therefore purely moving relative to one another. Therefore, there is no cell-related wear associated with bending the substrate.

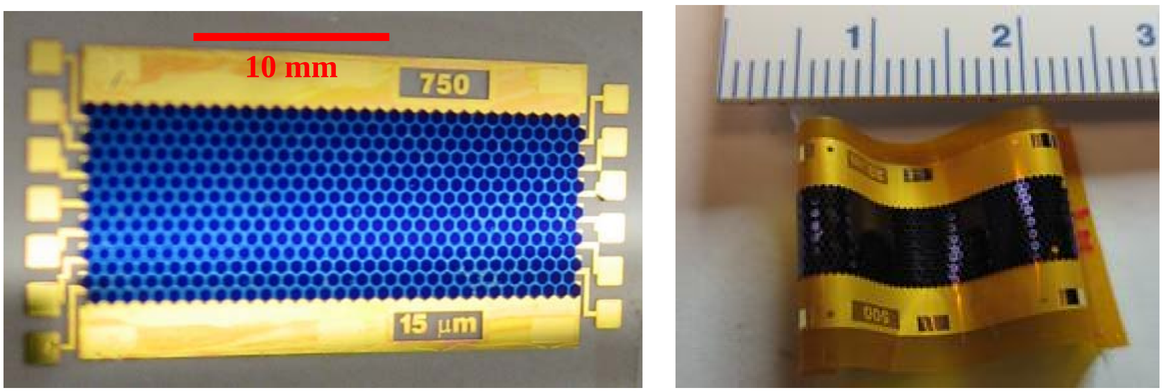

Figure 4: Photograph of MEPV modules implemented on both rigid (left) and flexible (right) substrates. The ruler to the right has units of cm. The flexible substrates have been demonstrated to have a bending radius down to 1 mm. The interconnection between the cells can be made on the substrate to satisfy the voltage and current requirements of the application, enabling mass fabrication of identical MEPV cells for different power requirements.

The resulting device utilizes several scaling advantages that match the requirements for remote, portable power described in the introduction. The thin geometry of the cell results in less travel distance for carriers before they are harvested, which results in lower bulk recombination. A significant number of individual cells can be placed in a reduced area due to the small lateral dimensions, leading to high power (450 W/kg) and voltage (1000 V/cm^2) for a given unit area and weight [5]. The reduced thickness also results in decreased material costs, since the handle wafer can be reused to fabricate more MEPV cells. Additional details on the fabrication and design of MEPVs can be found in [4]–[7].

1.2. Failure Analysis Techniques Overview

The tools used in this report fall into three broad categories. The first is the conventional electrical test that measures the current versus voltage (IV) of the device. The second is electroluminescence (EL) or light emission microscopy (LEM), which images the photons emitted when the device under test is placed under bias. The third includes variants of scanning laser microscopy techniques, where a laser raster scans the device and the resulting power consumption or generation is monitored and plotted as a function of laser position. The differences between the laser microscopy techniques include the wavelength of the incident light, the presence of bias, and whether or not the resulting signals are filtered.

Figure 5 outlines the components of an EL system, which consists of a power source and a sensitive imaging camera. The device under test is biased with the power source in a dark box and the photons that are emitted are captured by a charge-coupled device (CCD) camera that is thermoelectrically cooled to -75^{o}C. In the case of MEPV, the device can be either forward or reverse biased. Since silicon has an indirect band gap, long exposure times on the order of 150 to 180 seconds are typically required to generate the EL image. Therefore, if the field of view is limited, EL can be a slower process than laser scanning microscopy.

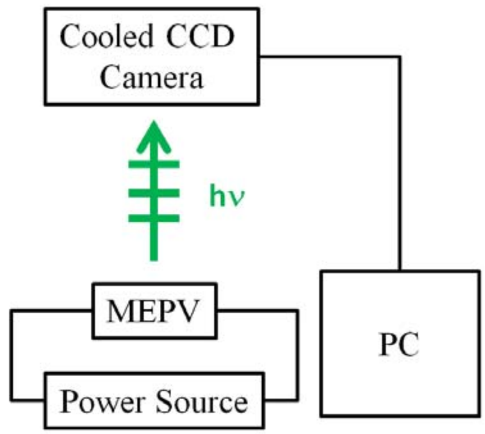

Figure 5: Configuration for electroluminescence (EL), which is also referred to as light emission spectroscopy (LEM). The device under test is biased by a power source and the resulting emitted photons are collected with a charge-coupled device (CCD) camera that is thermoelectrically cooled to -75^{o}C. The device can be either forward biased or, in the case of high leakage, reverse biased by the power source.

A summary of the vairous components in the laser scanning microscopy techniques in this project is provided in Figure 6. The left portion of the figure outlines the configuration for light induced voltage alteration (LIVA) and thermally induced voltage alteration (TIVA). The right portion describes the configuration for optical beam induced current (OBIC) and Seabeck effect imaging (SEI). In the case of LIVA and TIVA, the device is biased with a constant current source. The resulting voltage as the laser raster scans across the device is passed through an alternating current (AC) filter and the resulting signal is plotted as a function of laser position. In the case of OBIC and SEI, the device remains unbiased and is instead connected to a sensitive, low-noise preamplifier. As the laser raster scans the device, the resulting current generation is sent to a direct current (DC) amplifier that is plotted as a function of the laser position. In summary, the primary difference between LIVA/TIVA and OBIC/SEI is the presence of a bias (yes for LIVA/TIVA, no for OBIC/SEI) and the filtering scheme of the signal that is plotted (AC for LIVA/TIVA, DC for OBIC/SEI).

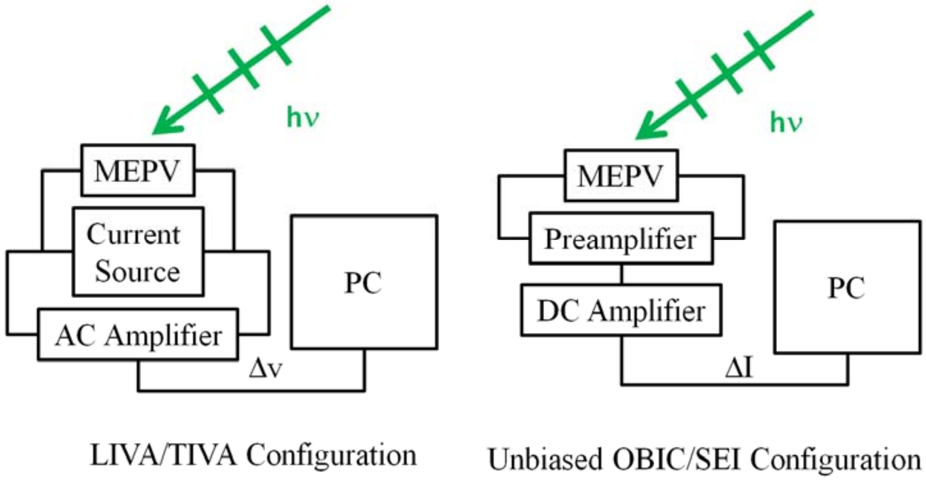

Figure 6: Configuration for light induced voltage alteration (LIVA, left), thermally induced voltage alteration (TIVA, left), unbiased optical beam induced current (OBIC, left), and unbiased Seabeck effect imaging (SEI, left). In all cases, a laser beam is raster-scanned across the device while the power consumption or generation is monitored and plotted as a function of beam position. The primary difference between LIVA/TIVA and OBIC/SEI is the amplification scheme, DC versus AC, and the presence of a biasing source in the case of LIVA/TIVA. In addition, LIVA and OBIC uses lasers with photon energy greater than the device band gap, resulting in the photoelectric effect. TIVA and SEI, in comparison, uses lasers with photon energy less than the device band gap, which induces thermal effects.

The difference between LIVA and TIVA is the same as the differentiating feature between OBIC and SEI: the wavelength of the incident laser light. In the case of LIVA and OBIC, a laser with photon energy above the device band gap is used to stimulate the MEPV cell, which is silicon in the case of this study. The laser creates electron-hole pairs when incident upon a diffusion region that change the power consumption or generation of the device under test. As a result, the resulting signal is a result of the photoelectric effect. The wavelength of the laser used for LIVA and OBIC is 543 nanometers (nm). In contrast, TIVA and SEI uses a laser with photon energy below the band gap of the device. As a result, the power characteristics of the device is altered through thermal effects, such as changes in resistance of narrow current paths or field gradients resulting from the Seabeck effect. The wavelength of the lasers used for TIVA and SEI are 1064 nm and 1340 nm.

Additional details on these fault localization techniques are described in greater detail in [8]. The subsequent sections in this report describe the adjustments made when applying the methods in this section to MEPV and summarize their PV-specific applications.

2. FAILURE ANALYSIS TECHNIQUES IN MEPV

This section provides additional details on the adaptation of CMOS defect localization techniques to MEPV. In addition to providing examples, each description also includes potential applications in MEPV development and manufacturing.

A majority of the results in this section are published in [9], [10], and the highlights are briefly reviewed here.

A summary of the techniques in this section and their applications are shown in Table 1:

Table 1. Summary of Characterization Methods for MEPV

Technique	Description	Information Provided
Electrical Testing	Current vs. voltage measurement of the device in the dark	Leakage current
Electroluminescence (Forward Bias)	Collecting emitted photons with a thermally cooled camera while device is under forward biased.	Cell functionality and relative performance
Electroluminescence (Reverse Bias)	Collecting emitted photons with a thermally cooled camera while device is under reverse biased.	Localize high reverse-bias leakage current and identify damage resulting from avalanche breakdown.
LIVA	Monitoring amplified AC voltage output while raster-scanning biased device with a laser stimulus that has photon energy above the band gap.	Rapid evaluation of cell functionality and relative performance. More sensitive than EL and faster than OBIC, though with less fidelity.
OBIC	Monitoring amplified DC current output while raster-scanning unbiased device with a laser stimulus that has photon energy above the band gap.	Evaluation of cell functionality and relative performance. Slower speed but improved fidelity compared to LIVA.
TIVA	Monitoring amplified AC voltage output while raster-scanning biased device with a laser stimulus that has photon energy below the band gap.	Verification of electrical connectivity of nonfunctioning cell, evaluation of contacts between metal layer and doped regions. Different contrast than SEI.
SEI	Monitoring amplified DC current output while raster-scanning unbiased device with a laser stimulus that has photon energy below the band gap.	Verification of electrical connectivity of nonfunctioning cell, evaluation of contacts between metal layer and doped regions. Different contrast than TIVA.

Section 2.1 focuses on the application of electroluminescence on MEPV. Section 2.2 examines laser scanning microscopy techniques that use photon energies above the band gap and provides a comparison on the relative advantages of LIVA and OBIC. Section 2.3 describes the use of below band gap laser scanning microscopy techniques, TIVA and SEI, to evaluate the contacts that connect the IBC to the silicon layer.

2.1 Electroluminescence Applications to MEPV

EL can be straightforwardly adapted to MEPV with virtually no adjustment from its CMOS application. Its application is identical to EL in traditional PV: it evaluates device functionality and performance when the device is under forward bias, and localizes leakage current when the device is under reverse bias. The primary difference between CMOS EL systems with traditional PV EL systems is the higher magnifications available at the expense of the reduced field of view.

Figure 7 provides an EL image of an MEPV module under forward bias that contains functioning cells as well as one non-functioning cell and one partially working MEPV cell. An applied voltage bias greater than the 0.7 Volts (V) per row of MEPVs is necessary to ensure turn-on and photon emission. Due to the large number of cells and forward bias configuration, high currents, up to 0.2 amperes (A) per MEPV cell in parallel, are necessary when performing EL to MEPV modules such as those shown in Figure 4.

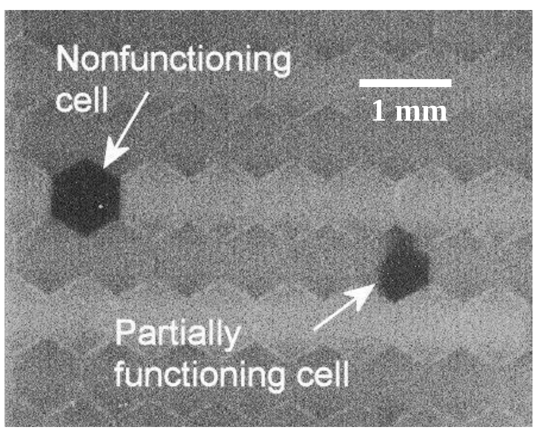

Figure 7: EL image of an MEPV module under forward bias, demonstrating its ability to identify a non-functioning cell and a partially functioning cell (labeled).

Differences in series resistance are an observed source of performance variation between MEPV cells. One potential cause for increased series resistance is the presence of voids in the solder connection between the electroplated copper and the substrate. These voids were identified through mechanically polished cross sections and can be eliminated by optimizing the heating and cooling of the solder during packaging. Figure 8 shows a cross section of an MEPV cell with voids present in the solder.

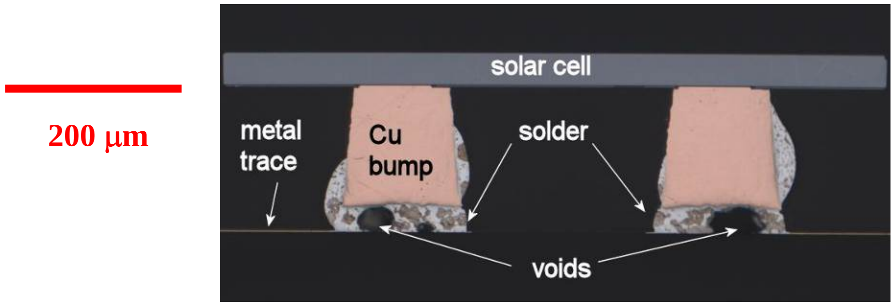

Figure 8: Subsequent analysis of samples with poor EL signals found a potential cause to be due to the presence of voids in the solder resulting in increased series resistance.

Functioning MEPV cells with low leakage currents do not produce detectable light emission signals under the current EL configuration. This conclusion is based on EL measurements with reverse bias voltages up to 30 V and exposure times up to 300 seconds. In the presence of current-induced dislocation paths, however, reverse bias EL can be used to localize the leakage. When subjected to damage associated with avalanche breakdown, the leakage current can generate efficient, microplasma-induced photons that can be captured by EL [11], [12].

Figure 9 is a bright field image of an MEPV cell with the reverse bias emission, shown in a green false color, overlaid on top. The emission is more robust than forward bias EL of working cells, which typically require 150 to 180 seconds of exposure. Reverse bias EL image in this case required only 15 seconds of exposure. Therefore, the reduced exposure time enables EL to be used as a tool to identify whether significant damage associated with avalanche-breakdown occurred.

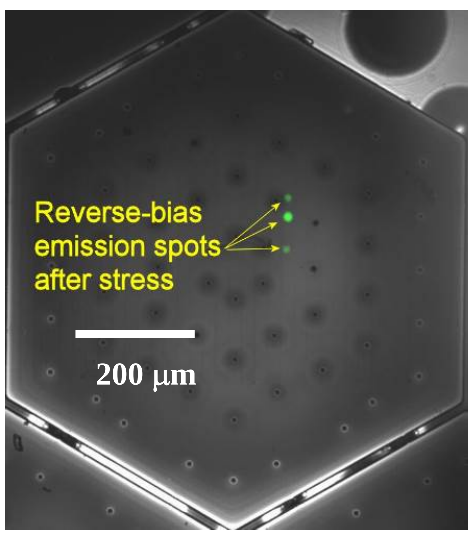

Figure 9: EL image of an MEPV module under reverse bias (green, false color) overlaid on top of the bright field image. The defects shown represent thermal runaway damage caused by excessive reverse bias stress.

2.2 Comparison of LIVA and OBIC for MEPV Evaluation and Screening

While both LIVA and OBIC can evaluate MEPV cell performance, the AC filtering of LIVA and the DC nature of OBIC provides different detection capabilities. The AC filtering of LIVA enables the detection of changes in diffusion regions with faster laser scan speeds. The increased scan speeds come at the cost of decreased spatial resolution. A good LIVA image, therefore must find the balance between scanning sufficiently fast to bring out contrast but not so fast as to result in excessive blurring or smearing. OBIC, in comparison, generates progressively more refined images as the scan speed decreases, and is therefore capable of creating more detailed images at the cost of increased imaging time.

Figure 10 shows an example of the difference between LIVA and OBIC when interrogating a cell that has non-uniform performance. The left side shows a LIVA image with a pixel dwell time of 61.4 μsec/pixel. The bright contrast in the cell area relative to the darker surroundings indicate carrier generation due to the laser stimulus and thus cell functionality. There is a bleed-over artifact in the lower-left corner of the MEPV cell as the laser transitions from a non-carrier-generating portion of the module into a functioning cell. Outside of this bleed-over artifact, the performance of the cell seems uniform.

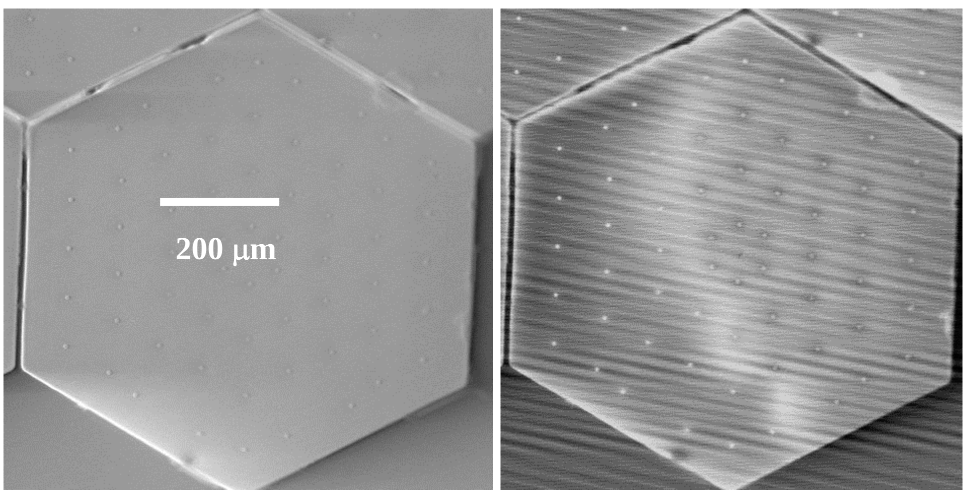

Figure 10: A comparison between the LIVA image (left) and the OBIC image (right) of a cell with uneven performance. The cell appears normal in the LIVA image. The OBIC image, however, is able to produce a different contrast between the regions of good performance (right half) and poor performance (left half). This contrast is removed by the AC filter in the LIVA configuration.

The right side of Figure 10 shows an OBIC image of the same cell, which shows that the left half of the cell is performing differently than the right half. LIVA was not able to detect this discrepancy because the change in contrast occurred too slowly and was removed by the AC filter. While a faster scan speed would bring out this contrast, it would also cause image blurring and worsen the bleed-over artifact, which would continue to mask the defect. Since OBIC does not have an AC filter, a slower scan speed of 123 μsec/pixel could be used to produce a sharp image while detecting the performance difference between the two parts of the cell.

While OBIC does not have the LIVA tradeoff between spatial fidelity and sensitivity, it still requires careful optimization of parameters, especially the attenuation of the scanning laser. Proper attenuation brings out the defects that would otherwise be drowned out by larger amounts of carrier generation induced by incident higher laser powers. This adjustment, however, comes with a tradeoff of greater DC amplification requirements and lower signal-to-noise ratio in the resulting signal. Figure 11 gives another example where OBIC is used to detect minute differences in performance between MEPV cells in a module.

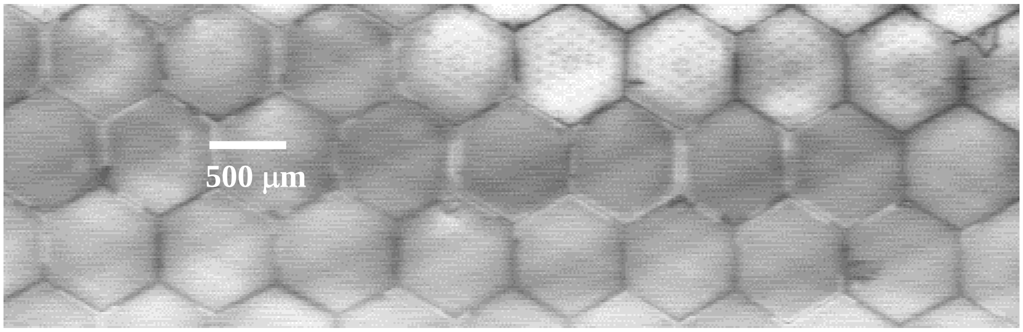

Figure 11: Another example of OBIC's ability to detect minor differences in MEPV cell performance in a module.

In addition to the dependence on choosing the appropriate scan speed, the ability of LIVA to detect performance differences between MEPV cells is also dependent on the scan direction. In the case of MEPV modules, however, two separate scans in orthogonal directions to each other should uncover any significant amount of cell-to-cell variation. Figure 12 shows an MEPV module where the horizontal rows, which are connected in parallel, have unequal performance. In the image, the laser beam scans in a horizontal, row-to-row book-style fashion. The performance difference between each row is filtered out by the AC filter and the resulting image falsely suggests fairly uniform performance.

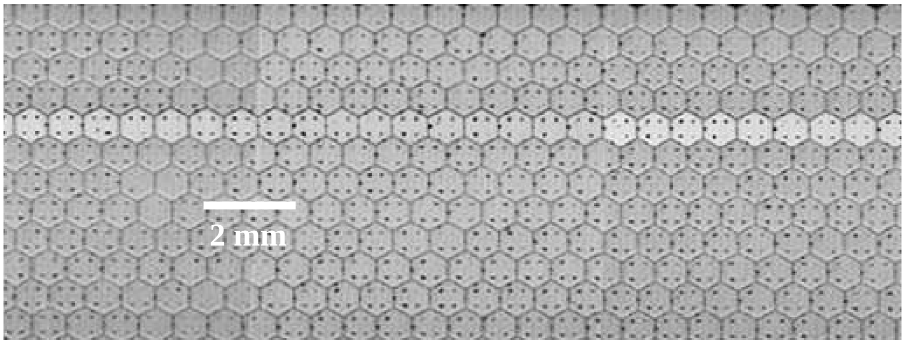

Figure 12: A demonstration of LIVA with a horizontal scanning direction, which is unable to detect differences between the various rows of MEPV cells. Each of the cell rows in this picture are connected in parallel, which are then connected to each other in series. The contrast change when the laser beam moves from one MEPV row to the next occurs too slowly and is removed by the AC filter.

When rotating the laser scanning direction by 90^o, however, the changes between rows occur faster and are not removed by the AC filter. The resulting image is shown in Figure 13, where the row-to-row variation of the module is evident. OBIC does not have this issue because the signal does not pass through an AC filter. As a result, each pixel produces a relative brightness that is not strongly dependent on pixel dwell time. Images of the same device using OBIC are virtually identical to Figure 13 in both horizontal and vertical scan directions.

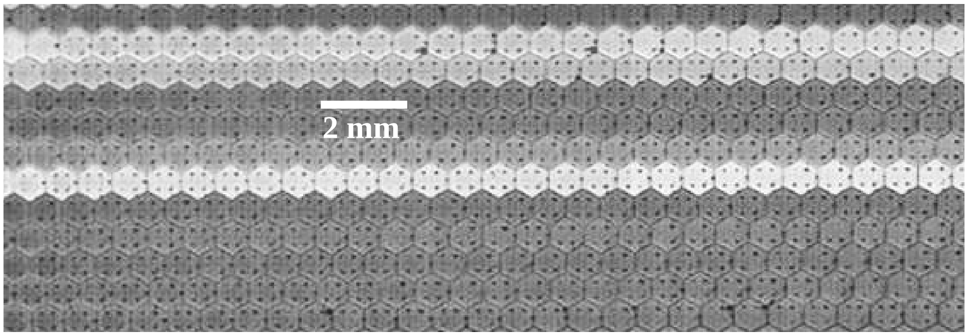

Figure 13: A LIVA image of the same array with the scanning direction rotated 90 degrees. The difference in performance from one row to the next is now readily apparent. OBIC produces a similar image regardless of scan direction, since there is no AC filter to remove slow transitions in power generation. LIVA could still be the preferred tool for screening applications, however, due to the increased scan speed compared to OBIC.

The speed of LIVA, however, makes it a potentially effective screening tool for MEPV production. In addition, the AC filtering of LIVA can provide additional information on how the cell is connected to the module. Figure 14 provides an example of an MEPV cell that was incorrectly connected when using a prototype pick-and-place tool for the final packaging step. The LIVA signal was raster-scanned book-reading style in this image. All correctly connected MEPV cells had a bright left edge and a dark right edge as the laser entered and exited the photogeneration regions. The incorrectly connected cell, which was nonfunctioning, still provided a LIVA response but had a *dark* left edge and a *bright* right edge, indicating a flip in polarity.

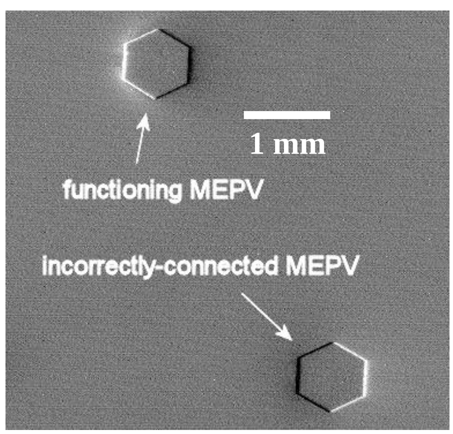

Figure 14: Contrast change in LIVA is enhanced by the AC filter when the laser beam crosses an MEPV cell and provides information on its electrical connectivity. The defective cell has a LIVA response. When comparing the image to that of a functioning MEPV cell, however, the location of the dark edge and light edge is switched. This observation reveals that the defective cell is connected in reverse by the pick-and-place assembly process.

In summary, OBIC with a scan speed of 123 μsec/pixel or slower provides the most information on both the relative performance of MEPVs but also any variations within an individual cell. LIVA can also provide similar information but requires an optimal pixel dwell time or scan speed to balance the tradeoff between spatial fidelity and contrast. In addition, the correct scan direction must be used to determine the performance differences in a given direction. The increased imaging speed of LIVA, however, makes it a potential screening tool to evaluate the performance uniformity of MEPV modules, which has been correlated with overall module performance. Therefore, both LIVA and OBIC can serve different purposes in MEPV technology and manufacturing development: LIVA for rapid evaluation or screening, OBIC for detailed, localized evaluation.

2.3 TIVA and SEI for MEPV Contact Defect Localization

Unlike LIVA and SEI, the difference in the effectiveness between TIVA and SEI is not as significant. The primary demonstrated application of TIVA and SEI is to evaluate the contacts that connect the IBC metal layer to the silicon. Since these contacts form narrow current paths, Seabeck effect currents generated by thermal gradients from the laser stimulus appear in both TIVA and SEI images. The small physical dimensions means that the TIVA/SEI signals vary quickly in time. As such, the TIVA/SEI signal is much more able to pass through the AC filter than the LIVA/OBIC signals. Therefore, other than contrast differences, the TIVA and SEI images are very similar.

TIVA and SEI images are formed by current changes caused by thermal stimulation instead of photogeneration, which is the case of LIVA and OBIC. Therefore, the presence of a TIVA/SEI signal verifies the presence of an electrical path from the MEPV cell to the rest of the module. This outcome allows evaluation of the connectivity of the MEPV independent of the cell’s ability to generate and harvest electron-hole pairs. Regions between two different materials create TIVA/SEI signals, such as the etch release holes and the contacts.

When combining the TIVA/SEI image with the known locations of contacts, the functionality of these contacts can be verified. Figure 16 shows an example of a TIVA image of an early MEPV design. The bright white dots show the strong contrast created from working contacts in the TIVA/SEI signal. The defective contacts can then be identified for further analysis. The presence of the TIVA/SEI image also verifies that the MEPV cell is electrically connected to the rest of the module, thus confirming the success of the packaging process.

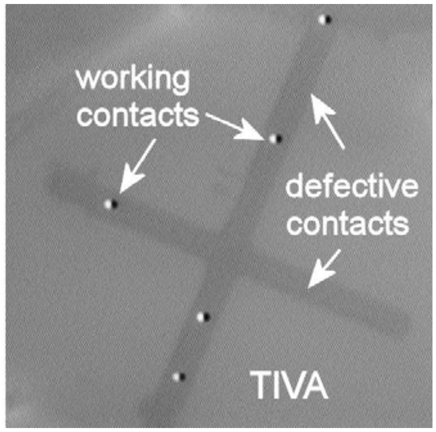

Figure 15: Both TIVA and SEI are capable of detecting the narrow current paths formed by the contacts that connect the doped silicon regions the metal layer below. When combined with knowledge of the expected locations of the TIVA/SEI signal, the technique can then be used to identify defective contacts.

Figure 16 shows a scanning electron microscopy (SEM) image of a focused ion beam (FIB) cross section of one of the defective contacts in Figure 15. In this case, the root cause of the defective contact was an overetch of the silicon, which electrically separated the contact and IBC metal layer from the silicon. After processing refinements, defective contacts are not a significant occurrence in MEPV fabrication.

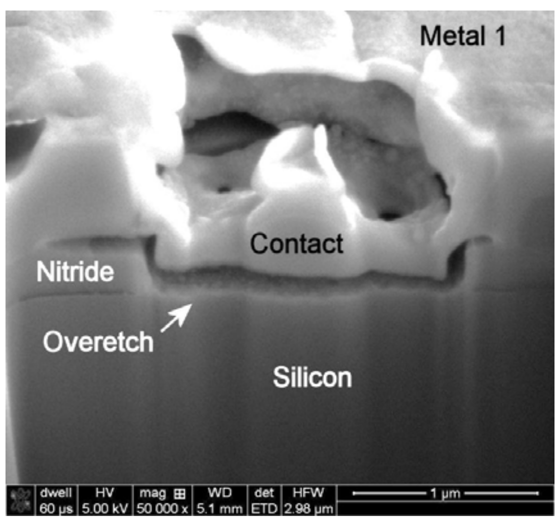

Figure 16: Scanning electron microscopy (SEM) image of a focused ion beam (FIB) cross section of a defective contact. The root cause was identified to be an overetch that electrically separated the contact and metal layer from the silicon below.

In summary, a number of CMOS defect localization tools were successfully adapted for the characterization of MEPV modules. EL under forward bias can directly evaluate the functionality and relative performance of MEPV cells. In cases where high reverse bias leakage is present, reverse bias EL can be used to localize the leakage path as well as identify the cause as damage associated with avalanche breakdown when the exposure time necessary to capture the signal is low.

Techniques based on laser scanning microscopy were also used to evaluate and troubleshoot MEPV modules. OBIC was found to provide the most detailed information on the relative localized performance of MEPV cells. While LIVA provides similar information with less fidelity due to the presence of an AC filter, its increased speed makes it suitable as potential fabrication and manufacturing screening tool. When using LIVA, however, two images with orthogonal laser scanning directions should be performed acquire the most complete picture.

Both TIVA and SEI produce similar images with different contrasts. Despite this overlap, the use of both configurations is recommended when possible, since some defects may show up better in one type of contrast than the other. TIVA and SEI can be used to verify the electrical connectivity of MEPV cells independently from the ability to generate electron-hole pairs. In addition, both techniques can be used to evaluate and troubleshoot the contacts that connect the silicon to the IBC metal layer.

3. APPLICATION OF REVERSE BIAS AND LIGHT STRESS ON MEPV

The studies in this section examine the effects of reverse bias and light-induced stress on MEPV cells. When a PV module experiences partial shading, the cells involved experience reverse bias voltage stress, which leads to degradation and diminished performance [13]. Thermal damage can occur in the event of avalanche breakdown, resulting in significant leakage currents in subsequent operation. Light-induced degradation has also been observed in single-crystalline, Czochralski-grown, boron-doped, silicon after prolonged exposure to energetic photons [14]. The exposure results in the formation of boron oxide complexes and iron-boron pairs that further lowers the efficiency of PV modules.

The results in the following subsections show that MEPV has good robustness to both reverse bias stress and light-induced degradation. Reverse bias breakdown did not occur until application of voltages beyond 75 volts. A prolonged application of sub-breakdown voltages produced only a nominal increase in leakage current, roughly double over the course of 600 hours. Extended exposure of MEPV cells to a purple laser with a wavelength of 405 nm produced no measureable changes in the reverse bias IV curve and slight changes in the forward bias traces, with a change of 5% at 0.7 V.

A further summary of the findings in this section can be found in [10], [15], [16].

3.1 MEPV Reverse Bias Stress to Breakdown

The MEPV modules were expected to have good robustness to reverse bias stress due to the p-i-n device geometry. The presence of a large intrinsic region should result in good resilience, though the extent had not been characterized prior to this study. As a first step, we quantified the reverse-bias voltage necessary to induce avalanche breakdown, and determined the number of events necessary to create permanent change in the leakage characteristics.

Figure 17 shows the effects of repeated breakdown in 28 MEPV cells connected in parallel subjected to reverse-bias voltage sweeps until breakdown occurred. These voltages were repeatedly applied until a significant (100×) increase in leakage current was detected. The plot shows that breakdown did not occur until voltage levels exceeding 75 V. Voltage sweeps between 0 and 80 V, which took approximately 10 seconds, did not substantial increases in leakage current until the 11th run. The IV-curves remain similar beyond -74V after this damage occurred, suggesting that the source of leakage currents at extremely high voltages is not significantly affected by the new failure. Further sweeps also produced no observable additional damage, since the existing leakage site and damaged cell serves as a current path for subsequent stresses, therefore serving as protection to the undamaged cells.

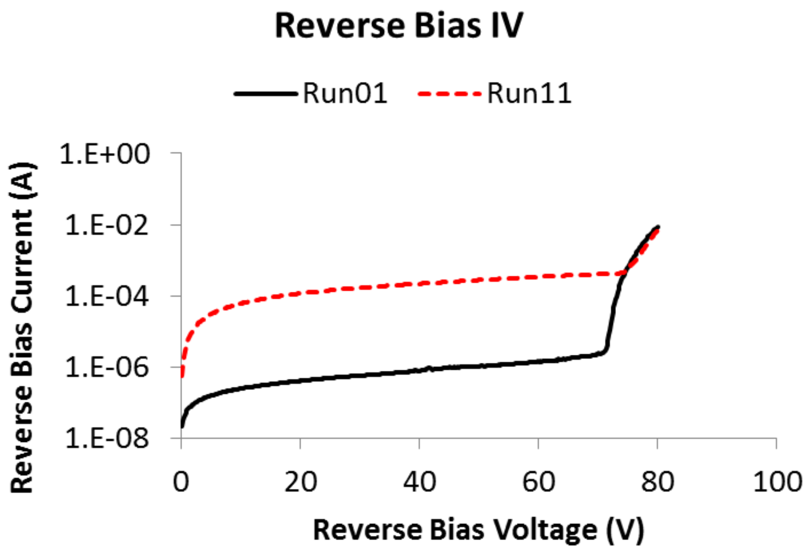

Figure 17: Reverse bias current as a function of applied voltage in stress-to-breakdown tests. The reverse bias current remained the same until the 11th run, after which it increased by two orders of magnitude due to thermally-induced damage creating new leakage current paths.

Subsequent analysis using EL, OBIC, TIVA, and SEI identified the location of the newly formed leakage site. The leakage was caused by excessive localized thermal runaway damage. Sample images are shown in Figure 18. Both forward biased EL and OBIC produced images similar to the OBIC measurement in the left picture, where a dark, non-functioning striped region was observed on one of the MEPV cells. Further imaging with TIVA and SEI identified damaged contacts and leakage paths, as shown in the right image.

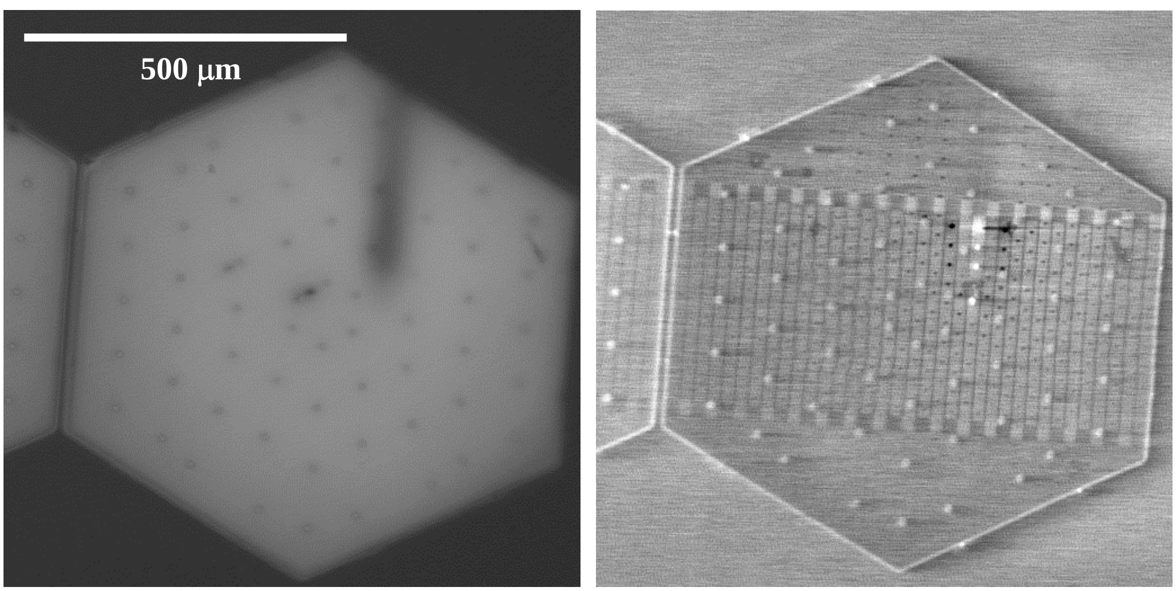

Figure 18: OBIC (left) and TIVA (right) images of the MEPV cell that was damaged due to repeated reverse bias breakdown tests. The damaged portion is readily visible in the OBIC image. The leakage path and damaged contacts can be detected using TIVA.

3.2 Reverse Bias Degradation of MEPV without Breakdown

This subsection describes the effects of prolonged exposure to lower levels of reverse bias stress that do not result in avalanche breakdown. Figure 19 shows 300 reverse bias measurements of 34 MEPV cells connected in parallel. Data was taken every two hours during 600 hours of 50 V reverse bias stress. The color transition from blue to red indicates the relative chronological order of each IV sweep, with blue representing the earlier measurements and red being the last ones. Labels on the left side of the plot provide approximations to the duration in which the stress has been applied prior to each IV measurement.

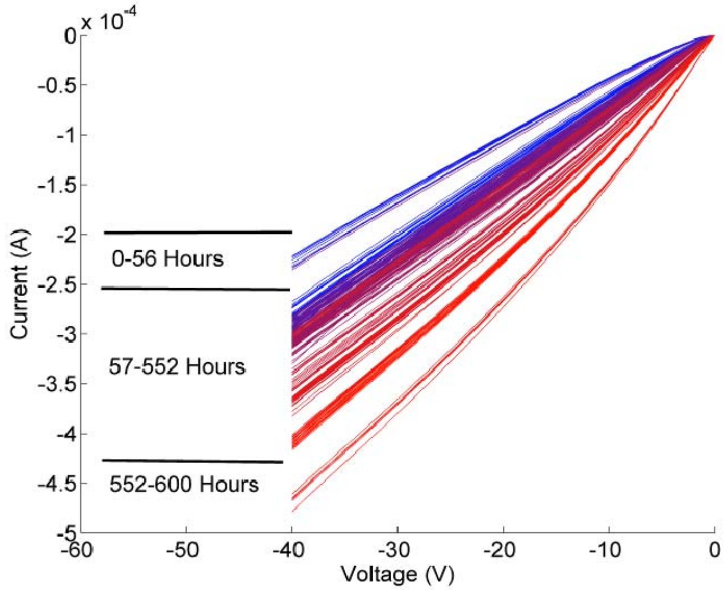

Figure 19: Reverse bias current-voltage (IV) curves of an MEPV module undergoing 600 hours of reverse bias stress at 50V. A steady decrease in reverse bias leakage is observed, with a doubling of reverse bias leakage at the end of testing.

The current leakage roughly doubled to 15 microamperes (μA) at -40 V. Unlike the stress-to-breakdown experiments of the previous section, the transition to increased leakage current was gradual and continuous. Figure 20 shows an example of identified damaged regions using forward bias EL. Subsequent localization of the leakage paths using reverse bias EL, TIVA and SEI were not successful and are the subject of further study.

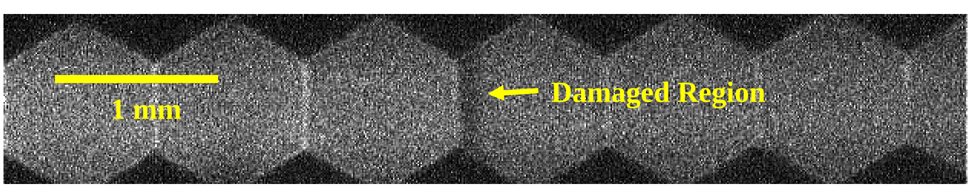

Figure 20: EL image of MEPV cells that have experienced prolonged reverse bias voltage stress without breakdown. Damage was found to be regional and at the edge of MEPV cells.

The absence of localized leakage paths similar to those detected by TIVA in the stress-to-breakdown suggests a different failure mechanism than thermal runaway damage associated with avalanche breakdown events. Therefore, it is recommended that further study to quantify this degradation mechanism focus on reverse bias voltages of 60 V or less in order to avoid convolution of avalanche breakdown effects.

3.3 Light-Induced Degradation on MEPV

The accelerated stress of higher energy photons was implemented by exposing a row of MEPV cells connected in parallel to a laser diode operating at 405 nm. The laser emits 4.5 mW of power over an area of 2 mm by 3 mm, resulting in a power density of 750 W/mm^2. For comparison purposes, the one-sun AM1.5 spectrum has approximately 0.88 W/mm^2 assuming a 1 nm bandwidth. As such, this configuration should contain significant acceleration when compared to what is expected from terrestrial field use.

Figure 21 shows the reverse bias IV curve taken every two hours on a row of MEPV cells undergoing 500 hours of light exposure plotted on both a log scale (left) and linear scale (right). The coloring scheme follows that of the prior figures where the earlier measurements are plotted in blue and subsequent traces transition to red over time. No differences are observed in the log scale and the minor discrepancies shown in the linear scale are within range of instrumentation error. Therefore, the exposure to light has no visible effect on the reverse bias portion of the IV curve.

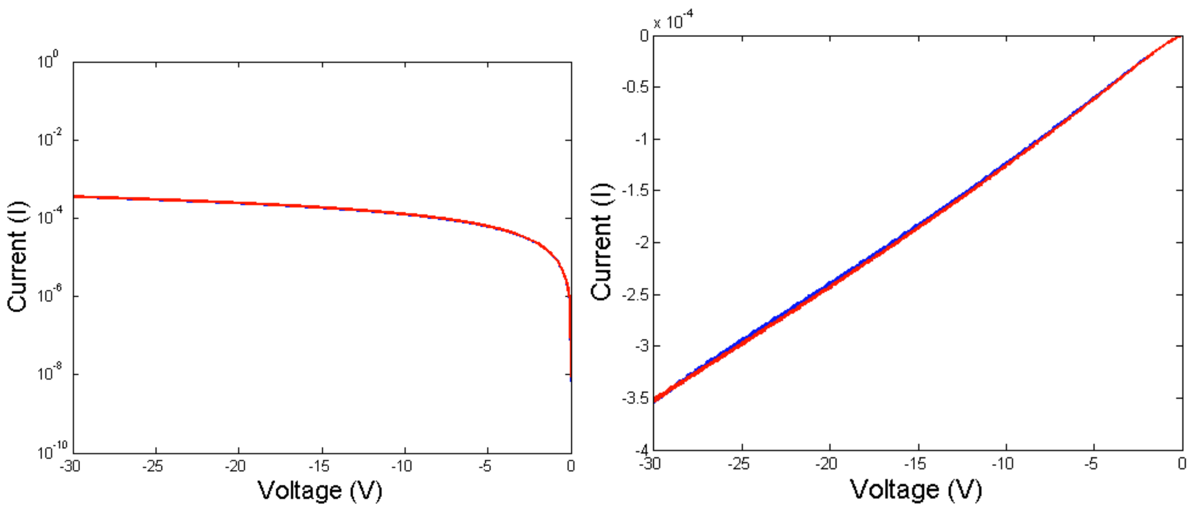

Figure 21: Reverse bias IV curve in a log (left) and linear (right) scale after light-induced degradation (LID) stress tests. No visible change in current is detected. The slight variation observed in the linear scale plot is within range of instrument error.

Figure 22 plots the corresponding forward bias characteristics over the time period in both a log (left) and linear (right) scale. The changes in the log scale between 0V and 0.1V are within instrument measurement error. There are detectable changes in the output current as the forward bias voltage increases.

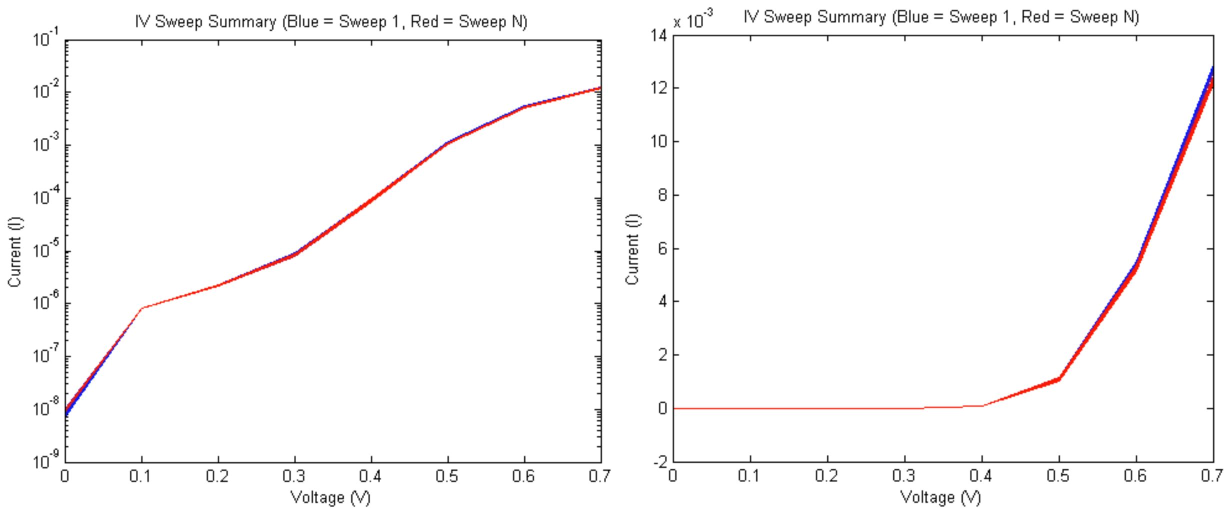

Figure 22: Forward bias in a log (left) and linear (right) scale of an MEPV module undergoing light-induced degradation (LID). The linear scale plot shows a slight decrease in the forward bias current at higher voltages, which could decreases the fill factor and efficiency of the MEPV module.

Figure 23 provides a closer look at the forward bias IV between 0.56 V and 0.7 V. A decrease in output current at these voltages is observed. After 500 hours of exposure, the output current decreased by approximately 5% at 0.7 V. This shift translates to decreased fill factor and efficiency, as a portion of the photocurrent output is hindered by the creation of impurity-related complexes.

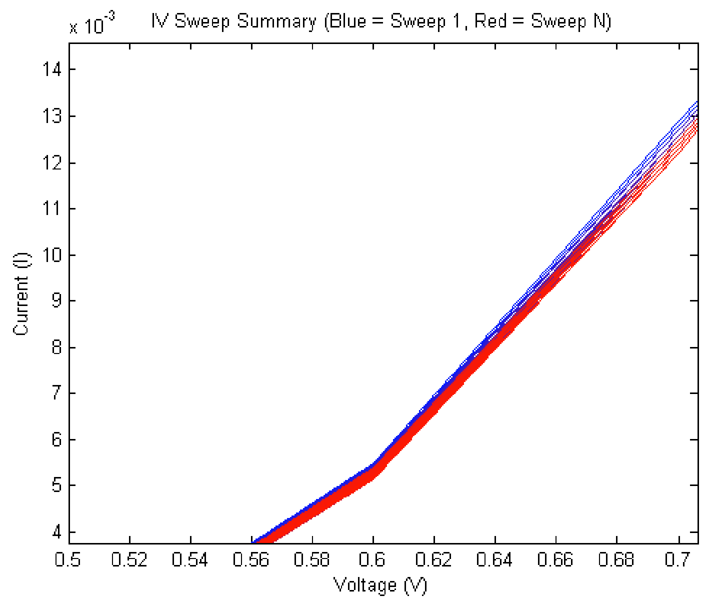

Figure 23: A closer look at the forward bias IV of the MEPV module undergoing light-induced degradation. A steady decrease in the amount of current generated under forward bias is shown, indicating a lower fill factor and cell performance.

In summary, three types of degradation were tested: reverse bias voltage stress until avalanche breakdown, reverse bias voltage stress without breakdown, and light induced degradation. The study found that MEPV has good robustness to reverse bias voltage, primarily due to the large regions of intrinsic silicon that separate the p-type and n-type areas. Breakdown did not occur until after 75V of reverse bias stress, and the cells tested were able to go through over ten avalanche breakdown events before significant changes in reverse bias leakage were detected. If breakdown was not reached, there is very slow degradation to the MEPV's reverse bias characteristics, where more than 600 hours of reverse bias stress at 50 V induced a roughly doubling of the leakage current at 40 V.

When subjected to light induced degradation, no changes in reverse bias characteristics were detected. After 500 hours of exposure, a slight decrease in the forward bias current was found, which will have minor adverse impacts to the module fill factor. The overall light-induced degradation was found to be minimal, likely due to lower concentration of impurities. A temperature dependence and additional statistics on the degradation due to differing levels of reverse bias is a topic of further study.

Overall, the MEPV responded well to the stress factors examined in this section. The exploration of additional stressors, such as temperature and humidity, as well as simultaneous application of stressors will provide more information towards lifetime predictive capability and design improvements for MEPV, further increasing its robustness.

4. CONCLUSIONS

The objective of the study described in this report is to develop the failure analysis infrastructure for further advancement in MEPV and similar microsystems-based photovoltaic technologies. In addition, the project also explores the effects of reverse bias voltage and light induced degradation to device IV characteristics.

The results found that, in general, CMOS failure analysis tools translate well to performing defect localization and evaluation of MEPV modules. EL under forward bias as well as LIVA using two different laser scanning directions are effective methods to determine the functionality of individual MEPV cells in a module. EL under reverse bias can be used to identify reverse bias current leakage paths if the damage resulted from avalanche breakdown. OBIC is a useful tool when higher resolution and detailed information is needed about localized photogeneration capability, though the additional fidelity comes at the price of slower speed. TIVA and SEI provide the ability to test the interconnectivity of the cell to the module independently of PV characteristics. In addition, TIVA and SEI can be used to troubleshoot contacts and identify leakage paths.

In addition, the effects of reverse bias and light-induced stress on MEPV were examined. Since the MEPV has larger areas of intrinsic silicon separating small distributed p- and n-doped regions, the modules were found to have good resilience to reverse bias stress. In addition, low impurities in the process results in resistance to light-induced degradation. Only a minor potential change in IV characteristics was observed after extensive exposure to power concentrations much greater than those observed in terrestrial applications.

Future development of MEPV technology will greatly benefit from the simultaneous development of device failure analysis and reliability. Many of MEPV’s advantages are a good match for power generation in remote locations. Therefore confidence in its long-term performance is of great importance. Suggested areas of importance of future work include expansion of the CMOS failure analysis techniques to multi-junction MEPVs or MEPVs with different material systems. Many of these tools should translate to new materials after adjustments to the new band gap values. The development of MEPV could also benefit from additional tools to trace current paths.

In regards to reliability, the testing with additional stressors, such as temperature and broadband light-induced degradation, will provide a more comprehensive view on overall long-term performance and uncover related obstacles. In addition, the study of simultaneous application of stressors, such as exposure to light stress while at elevated temperatures, will be needed to uncover interaction effects. It is our belief that the development of failure analysis tools and a reliability model addressing the questions above will further accelerate the maturation of MEPV technology.

6. REFERENCES

[1] H. Arase, A. Matsushita, A. Itou, T. Asano, N. Hayashi, D. Inoue, R. Futakuchi, K. Inoue, T. Nakagawa, M. Yamamoto, E. Fujii, Y. Anda, H. Ishida, T. Ueda, O. Fidaner, M. Wiemer, and D. Ueda, “A Novel Thin Concentrator Photovoltaic With Microsolar Cells Directly Attached to a Lens Array,” *IEEE J. Photovolt.*, vol. 4, no. 2, pp. 709–712, Mar. 2014.

[2] J. Yoon, A. J. Baca, S.-I. Park, P. Elvikis, J. B. Geddes, L. Li, R. H. Kim, J. Xiao, S. Wang, T.-H. Kim, M. J. Motala, B. Y. Ahn, E. B. Duoss, J. A. Lewis, R. G. Nuzzo, P. M. Ferreira, Y. Huang, A. Rockett, and J. A. Rogers, “Ultrathin silicon solar microcells for semitransparent, mechanically flexible and microconcentrator module designs,” *Nat. Mater.*, vol. 7, no. 11, pp. 907–915, Nov. 2008.

[3] K. J. Weber, A. W. BLAKERS, M. J. Stocks, J. H. Babaei, V. A. Everett, A. J. Neuendorf, and P. J. Verlinden, “A novel low-cost, high-efficiency micromachined silicon solar cell,” *IEEE Electron Device Lett.*, vol. 25, no. 1, pp. 37–39, 2004.

[4] G. N. Nielson, M. Okandan, J. L. Cruz-Campa, A. L. Lentine, W. C. Sweatt, V. P. Gupta, and J. S. Nelson, “Leveraging scale effects to create next-generation photovoltaic systems through micro- and nanotechnologies,” *Proc. SPIE*, vol. 8373, pp. 837317–837317, May 2012.

[5] J. L. Cruz-Campa, G. N. Nielson, M. Okandan, P. J. Resnick, C. A. Sanchez, J. Nguyen, B. B. Yang, A. C. Kilgo, C. Ford, and J. S. Nelson, “Ultra-thin single crystal silicon modules capable of 450 W/kg and bending radii <1mm: Fabrication and characterization,” in *Photovoltaic Specialists Conference (PVSC), 2013 IEEE 39th*, 2013, pp. 1218–1223.

[6] G. N. Nielson, M. Okandan, J. L. Cruz-Campa, P. J. Resnick, M. W. Wanlass, P. J. Clews, T. C. Pluym, C. A. Sanchez, and V. P. Gupta, “Microfabrication of microsystem-enabled photovoltaic (MEPV) cells,” *Proc SPIE 7927 Adv. Fabr. Technol. MicroNano Opt. Photonics IV*, p. 79270P–79270P, Feb. 2011.

[7] G. N. Nielson, M. Okandan, P. Resnick, J. L. Cruz-Campa, T. Pluym, P. J. Clews, E. Steenbergen, and V. P. Gupta, “Microscale c-Si (c)PV cells for low-cost power,” in *2009 34th IEEE Photovoltaic Specialists Conference (PVSC)*, 2009, pp. 001816 –001821.

[8] Electronic Device Failure Analysis Society, *Microelectronics Failure Analysis Desk Reference, 6th Ed.*, 6th ed. ASM International, 2011.

[9] B. B. Yang, J. L. Cruz-Campa, G. S. Haase, P. Tangyunyong, E. I. Cole, A. A. Pimentel, P. J. Resnick, M. Okandan, and G. N. Nielson, “Fault localization and failure modes in microsystems-enabled photovoltaic devices,” in *Reliability Physics Symposium (IRPS), 2013 IEEE International*, 2013, pp. 4B.2.1–4B.2.5.

[10] B. B. Yang, J. L. Cruz-Campa, G. S. Haase, P. Tangyunyong, M. Okandan, and G. Nielson, “Comparison of Beam-Based Failure Analysis Techniques for Microsystems- Enab31-led Photovoltaics,” in *Conference Proceedings from the 39th International Symposium for Testing and Failure Analysis*, San Jose, CA, United states, pp. 369–375.

[11] N. Akil, S. E. Kerns, J. Kerns, D.V., A. Hoffmann, and J.-P. Charles, “A multimechanism model for photon generation by silicon junctions in avalanche breakdown,” *IEEE Trans. Electron Devices*, vol. 46, no. 5, pp. 1022–1028, 1999.

[12] D. V. Kerns, K. Arora, S. Kurinec, and W. Power, “Si diode under avalanche breakdown as a light emitting source for VLSI optical interconnect,” in , *Twenty-First Southeastern Symposium on System Theory, 1989. Proceedings*, 1989, pp. 677–680.

[13] G. B. Alers, J. Zhou, C. Deline, P. Hacke, and S. R. Kurtz, “Degradation of individual cells in a module measured with differential IV analysis,” *Prog. Photovolt. Res. Appl.*, vol. 19, no. 8, pp. 977–982, 2011.
[14] J. Schmidt, “Light-Induced Degradation in Crystalline Silicon Solar Cells,” *Solid State Phenom.*, vol. 95–96, pp. 187–196, 2004.
[15] B. B. Yang, J. L. Cruz-Campa, G. S. Haase, P. Tangyunyong, M. Okandan, and G. Nielson, “Reliability model development for microsystems-enabled photovoltaics,” in *Photovoltaic Specialists Conference (PVSC), 2014 IEEE 40th*, Denver, CO, United states, 2014.
[16] B. B. Yang, J. L. Cruz-Campa, G. S. Haase, E. I. Cole, P. Tangyunyong, P. J. Resnick, A. C. Kilgo, M. Okandan, and G. N. Nielson, “Failure Analysis Techniques for Microsystems-Enabled Photovoltaics,” *IEEE J. Photovolt.*, vol. 4, no. 1, pp. 470–476, Jan. 2014.

Distribution

1	MS0359	D. Chavez, LDRD Office	1911
1	MS0899	Technical Library	9536 (electronic copy)
1	MS1081	Benjamin Yang	1755
1	MS1081	Guillermo Loubriel	1755

Sandia National Laboratories